RESEARCH ARTICLE

Key Points:
- Intraseasonal temperature variability is dominant in the vicinity of the thermocline
- CP El Niño is associated with an increase in intraseasonal equatorial Kelvin activity
- Intraseasonal Kelvin wave starts strongly dissipating around 120°W

Correspondence to:
K. Mosquera-Vásquez,
kobi.mosquera@igp.gob.pe

# The Central Pacific El Niño intraseasonal Kelvin wave

K. Mosquera-Vásquez[1], B. Dewitte[2], and Serena Illig[2]

[1]Instituto Geofísico del Perú, Lima, Perú, [2]Laboratoire d'Etudes en Géophysique et Océanographie Spatiales, Toulouse, France

Abstract In this study, we document and interpret the characteristics of the IntraSeasonal Kelvin wave (ISKw) in the Pacific over the 1989–2011 period, based on observations, a linear model, and the outputs of an Ocean General Circulation Model (OGCM). We focus on the wave activity during the Central Pacific (CP) El Niño events contrasting with the extraordinary El Niño of 1997/1998. We find that the ISKw activity is enhanced in Austral summer (spring) in the central Pacific (west of ∼120°W) during CP El Niño events. The linear model experiment indicates that the Austral summer peak is wind-forced, while the Austral spring peak is not and consequently results from nonlinear processes. In addition, a strong dissipation of the ISKws is observed east of 120°W which cannot be accounted for by a linear model using a Rayleigh friction. A vertical and horizontal mode decomposition of the OGCM simulation further confirms the sharp changes in characteristics of the ISKws as well as the reflection of the latter into first-meridional Rossby wave at the longitude where the maximum zonal gradient of the thermocline is found (∼120°W). Our analysis suggests that the confinement of CP El Niño warming in the central Pacific may result from the reinforcement of the zonal gradient in stratification associated with the La Niña-like conditions since the late of the 1990s, leading to scattering of the energy of the ISKws in the eastern Pacific.

1. Introduction

Recent studies have reported the existence of at least two types of El Niño events [*Ashok et al.*, 2007; *Kao and Yu*, 2009; *Kug et al.*, 2009]: one with anomalies peaking in the eastern Pacific (i.e., Eastern Pacific (EP) El Niño or cold tongue El Niño) like in 1997/1998, and one having its center of action in the central Pacific referred to as Modoki El Niño or Central Pacific (CP) El Niño (as referred hereafter) or warm pool El Niño. The exact nature and mechanism of the latter have been the subject of debate in the community [*Capotondi et al.*, 2014] due in part to its apparent increase in occurrence in recent decades [*Yeh et al.*, 2009; *Lee and McPhaden*, 2010] and the difficulty to interpret these two types of events as the expression of either two distinct regimes [*Takahashi et al.*, 2011] or a continuum in the ENSO variability [*Giese and Ray*, 2011; *Johnson*, 2013]. There have been also some difficulties in interpreting the recent El Niño events from current ENSO theories [*Xiang et al.*, 2013]. For instance, although *Ren and Jin* [2013] suggest that CP El Niño can be understood to a large extent by the recharge oscillator mechanism, *Kug et al.* [2009] indicate that CP El Niño are characterized by a weak recharge-discharge process and the phase relationship between the two dominant modes of the thermocline variability (i.e., the so-called tilt and warm water volume modes) has changed at the beginning of the 21st century [*McPhaden*, 2012]. In term of thermodynamical processes within the mixed-layer, CP El Niño events tend to be dominated by the zonal advective feedback in the central Pacific with a weak contribution from thermocline feedback in the eastern equatorial Pacific [*Kug et al.*, 2009; *Ren and Jin*, 2013]. On the other hand, CP El Niño events are also associated with equatorial Kelvin wave dynamics [*Dewitte et al.*, 2012a] that have the potential to produce anomalous vertical advection in the eastern Pacific [*Mosquera-Vásquez et al.*, 2013]. The former studies, however, do not explain why the SST warming remains confined in the central Pacific, calling for the investigation of other processes including nonlinear ones [*Xiang et al.*, 2013; *Dommenget et al.*, 2012]. The fact that the recharge-discharge process is weak during CP El Niño, implying that the ocean state prior to its development is weakly influential, suggests that CP El Niño evolution are more likely to be influenced by random atmospheric forcing during its development phase. Random atmospheric noise usually refers to the components of the Intraseasonal atmospheric Tropical Variability (ITV) [*Wheeler and Kiladis*, 1999] including the Madden Julian Oscillation (MJO) [*Madden and*
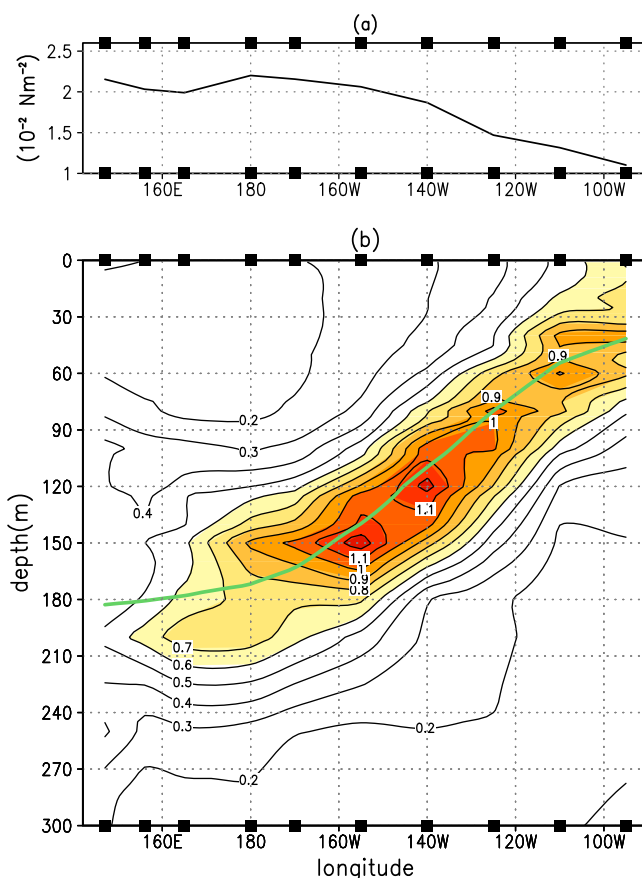
Figure 1. Root mean square (RMS) along the equatorial band (2°S–2°N) of the (a) intraseasonal zonal wind stress as a function of longitude (in 10^{-2} N m^{-2}) and (b) intraseasonal temperature as a function of longitude and depth (in °C) from TAO data for the period 2000–2011. The green thick line in Figure 1b indicates the mean thermocline depth (20°C isotherm depth). The squares on the longitude axis indicate the positions of the TAO mooring buoys.

Julian, 1972] and Westerly Wind Bursts (WWBs). The MJO and WWBs, however, may be influenced by the background oceanic state during ENSO [*Eisenman et al.*, 2005; *Roundy and Kravitz*, 2009; *Seiki and Takayabu*, 2007]. For instance, *Roundy and Kravitz* [2009] indicated that weather patterns, comprising those associated with MJO, tend to evolve differently in association with oceanic Kelvin waves during different phases of ENSO. These former studies are consistent with the notion that the ENSO-state dependence of the ITV serves as a source of stochastic forcing for ENSO [*Jin et al.*, 2007; *Kug et al.*, 2009]. The oceanic expression of the ITV is composed of the intraseasonal Kelvin wave (ISKw) that is forced by WWB and was shown to be influential for triggering strong EP El Niño events [*Bergman et al.*, 2001; *McPhaden et al.*, 2006]. In particular, the 1997/1998 El Niño was associated with two pulses of ISKw prior to its development [*Dewitte et al.*, 2003] which may have triggered the initial

warming in the central Pacific leading to the growth of the SST anomalies [*Lengaigne et al.*, 2004]. The 1997/1998 El Niño is rather peculiar because the peak activity of the ISKw took place ~6 months prior the El Niño peak [*Ramos et al.*, 2008], which reflects the strong seasonal dependence of the MJO/ENSO relationship (i.e., MJO peak variance being in May to June prior to the ENSO peak in November to December) described in former studies [*Hendon et al.*, 2007; *McPhaden et al.*, 2006].

Here we investigate the ISKw activity during CP El Niño events over the last two decades based on observations and model outputs. Our motivation is first to better understand its relationship with the CP El Niño development and decay, considering that the ISKw is influential on the spread of ENSO forecasts [*Wang et al.*, 2011] and that prediction systems exhibit a distinct forecast skill depending on the El Niño type [*Hu et al.*, 2012; *Xue et al.*, 2013]. We also aim at documenting some characteristics of the ISKw activity that cannot be inferred directly from the available observation data sets and sheding light on processes that may explain why CP El Niño events do not expand to the eastern Pacific and remain confined in the central Pacific. Former studies have largely contributed to better understanding the forcing mechanisms of the ISKw in the Pacific in particular exploiting TAO (Tropical Atmosphere Ocean project) and altimetry observations. For instance, *Cravatte et al.* [2003] used TOPEX/POSEIDON and TAO data to study the ISKws over the 1992–1999 period. They found that the ISKw characteristics (frequency, amplitude) could not be explained in a straightforward manner from linear theory. For instance, energy at $(120$ day$)^{-1}$ was found in the eastern Pacific that could not be attributed to wind forcing. They also noted a complex vertical structure variability associated with at least the first two baroclinic modes. Interestingly, the intraseasonal variability of temperature along the equator has also a fine vertical scale (Figure 1), with a peak amplitude in the vicinity of the

thermocline and a weak amplitude at the surface. Although the pattern of Figure 1b cannot be solely interpreted as resulting from ISKw, it is expected that vertical isotherm displacements near the thermocline along the equator will be to a large extent explained as resulting from the forced equatorial Kelvin wave [e.g., *Kessler et al.*, 1995; see also *Dewitte et al.* [2009] for the theoretical background]. Note that the variability decreases to the east of ∼120°W by a factor of 1.4 that is an indication of a marked dissipation. TAO data also revealed that intraseasonal variability in the range of frequencies [60–90 days]$^{-1}$ was also prominent in subsurface zonal current at 140°W and 110°W [*McPhaden and Taft*, 1988]. Most studies of the oceanic ISKw have argued that it is tightly linked to the MJO-induced wind stress anomalies [e.g., *Kessler et al.*, 1995; *Hendon et al.*, 1998; *Zhang*, 2001; *Roundy and Kiladis*, 2006; *Shinoda et al.*, 2008] and that it can act as a trigger of El Niño events [*Kessler and McPhaden*, 1995a, 1995b; *McPhaden*, 1999, 2002; *Kessler and Kleeman*, 2000; *Seo and Xue*, 2005]. However, the latter studies have focused on a period encompassing the strong 1997/1998 El Niño, for which there is a well-known delayed ENSO-MJO seasonal relationship [*Hendon et al.*, 2007; *McPhaden et al.*, 2006]. Recently, *Gushchina and Dewitte* [2012] have shown that the seasonal dependence of the ENSO-MJO relationship was distinctive during CP and EP El Niño events and that such difference between the two types of El Niño could reflect into the ISKw activity. They proposed in particular, that MJO activity is enhanced during the mature phase of the CP El Niño events, extending their persistence compared to EP El Niño events. This issue is worth tackling because it suggests that ITV and its oceanic expression might be tightly linked to the CP El Niño dynamics, rather than just acting as a noise maker for ENSO triggering. It calls for better understanding the ISKw dynamics during such type of ENSO event, that is, its forcing mechanism and dissipation process. This is the topic of the present paper that can be viewed as an extension of *Gushchina and Dewitte* [2012] focusing on the oceanic ISKw characteristics and its forcing mechanism. Of particular interest is the dissipation process associated with the horizontal anisotropy of the mean density in the upper thermocline. In the recent decades, the mean thermocline has been steeper due to La Niña-like conditions since the late of the 1990s [*Xiang et al.*, 2013]. Our analysis suggests that this may have favored scattering of energy of the ISKw, leading to a "trapping" of its energy in the central equatorial Pacific.

The paper is organized as follows: section 2 introduces the observed data sets and the ocean model outputs used in this study, as well as the methodology. Section 3 documents the characteristics of the propagating variability in both the observations and two models having different physics. Section 4 provides evidences of modal dispersion of the intraseasonal equatorial Kelvin wave in the eastern Pacific. Section 5 is a discussion of the results followed by concluding remarks and perspectives to this work.

2. Data and Method

The intraseasonal (IS) anomalies are estimated as the difference between the original data (either daily mean, 3 day mean or 7 day mean, depending on its source) and the filtered (1–2–1) monthly mean data interpolated at the temporal resolution of the original data. This methodology was suggested by *Lin et al.* [2000] to study intraseasonal atmospheric variability in the tropics and is similar to a high-pass filter with a transfer function characterized by a −1, −3, and −10 dB attenuation (79%, 50%, and 10% of the input power survives) at (117 day)$^{-1}$, (168 day)$^{-1}$, and (466 day)$^{-1}$, respectively. It has been used recently to study the intraseasonal oceanic variability in the upwelling systems of north Benguela [*Goubanova et al.*, 2013] and Peru [*Illig et al.*, 2014].

Interannual (IA) anomalies correspond to monthly mean data, which is smoothed with a 1–2–1 filter, relative to the mean climatology calculated over the period 1990–2011.

CP El Niño years are selected following *Yu and Kim* [2013], which leads to 1992, 1994, 2002, 2004, 2006, and 2009 as CP El Niño years. Note that the 2006 year is classified as a mixed-type El Niño year by *Yu and Kim* [2013]. However, we consider this event as a CP El Niño event considering its closer similarity to the other El Niño events of the record used in this study compared to the 1997 El Niño event. We will therefore contrast the characteristics of the CP El Niño events with the ones of the 1997/1998 El Niño that is clearly the only extreme El Niño event over the period of interest in this paper.

2.1. Sea Level Height From Altimetry
The gridded sea level anomaly (hereafter referred to as TPJ) data over the period 1993–2011 were supplied by AVISO/altimetry [*Ducet et al.*, 2000]. They were built using optimal interpolation of T/P and ERS data on a
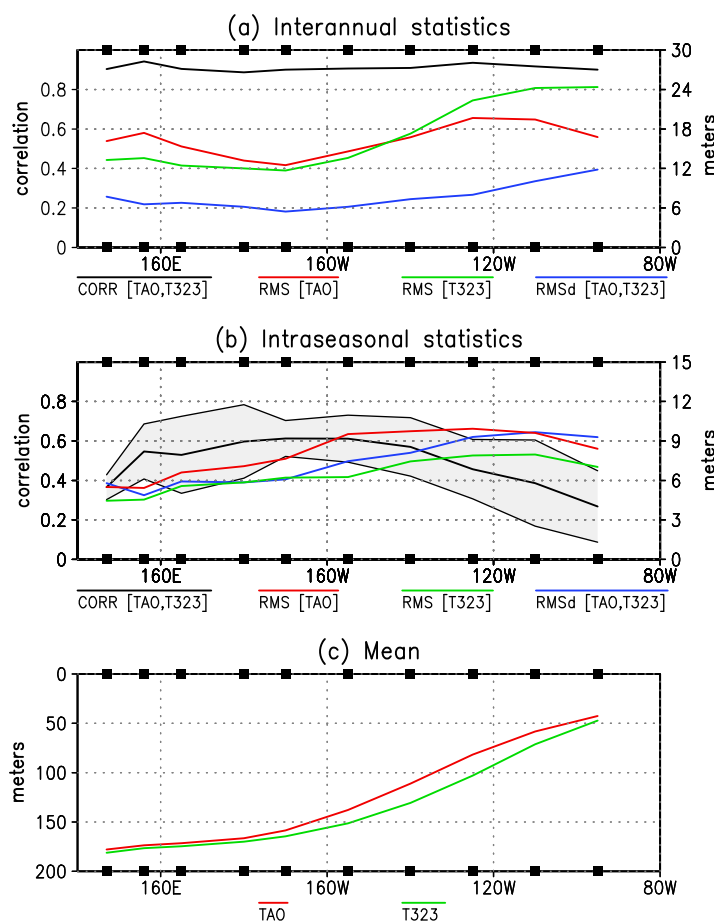
Figure 2. Validation of T323 from TAO data for the period 1990–2011: (left) correlation (black line) and (right) root mean square (RMS) difference (blue line) between observations and model for the thermocline depth (a) interannual and (b) intraseasonal anomalies. The RMS for observations and model is also displayed (red line for observations and green line for the model). The gray shading in Figure 2b provides the range of values of the correlation between model and observation over one calendar year taken within the period 1990–2011. (c) Mean thermocline depth for model (green) and observation (red). The squares on the longitude axis indicate the positions of the TAO mooring buoys. Units are in meters.

$1/4° \times 1/4°$ grid every 7 days. If a precision of individual instantaneous measurements is of the order of 6 cm Root Mean Square (RMS) [*Fu et al.*, 1994], errors on such gridded product have been estimated to 2–3 cm RMS for 7 day-averaged maps and spatial scales larger than 200 km [*Le Traon and Ogor*, 1998].

2.2. SST and 20°C Isotherm Depth From TAO

In this study, we also take advantage of the TAO data [*Hayes et al.*, 1991; *McPhaden et al.*, 1998], where the SST and 20°C isotherm depth are obtained from 29 mooring buoys (2°N, 0°, and 2°S at 147°E, 156°E, 165°E, 180°, 170°W, 155°W, 140°W, 125°W, 110°W, and 95°W). In order to fill gaps in the data, a vertical linear interpolation is first applied to each time series (daily mean data) and then a linear interpolation in the zonal direction is applied in order to fill data gaps only if both neighboring data are available. Then, a meridional mean (2°S, 0°, and 2°N) provides an estimated equatorial section without missing data. Note that some linear temporal interpolations are necessary, especially at 95°W. Such interpolation procedure is acceptable until 2011 when the density of the TAO data remains reasonable (above 60% at 100 m in the eastern equatorial Pacific) but cannot be performed beyond that date due to the maintenance suspension of the TAO array (density of data falls below ~25% at 100 m from 2012, see *Takahashi et al.* [2014], Figure 5.2). The limitations associated with the interpolation of the TAO data have motivated the use of a model simulation for the interpretation of the observational results.

2.3. The OGCM Simulation (T323)

The model product used in this work belongs to the set of MERCATOR global OGCM simulations (http://www.mercator-ocean.fr/). The configuration, referred to as T323, is an eddy-permitting 1/4° model with 50 vertical levels (whom 23 belong to the upper 100 m). It is based on the primitive-equation global OGCM Océan PArallélisé (OPA) [*Madec et al.*, 1998] and is developed at the Laboratoire d'Océanographie et du Climat: Expérimentations et Approches Numériques (LOCEAN, Paris, France). T323 was forced with 3 h (surface winds) and daily forcing (corrected precipitation and radiative fluxes only) from ERA-Interim. Here the experiment was initialized on January 1989 from rest and with temperature and salinity from Levitus data [*Levitus and Boyer*, 1994]. Since no spin-up is used, only intraseasonal to interannual variability will be discussed in the paper and the year 1989 is disregarded in the estimation of the reference climatology.

Table 1. Validation of Thermocline Depth Interannual Variability: Zonal Mean for RMS, Correlation, and RMS Difference Between T323 and Observations (TAO) at 147°E, 156°E, 165°E, 180°, 170°W, 155°W, 140°W, 125°W, 110°W, and 95°W (Mooring Locations)

Mean Correlation [T323,TAO]	Mean RMS [T323] (m)	Mean RMS [TAO] (m)	Mean RMS Difference [T323,TAO] (m)
0.91	17.0	16.3	7.7

Despite the fact that there is no data assimilation in this experiment, the model is skillful in capturing most aspects of the equatorial variability in the Pacific Ocean. In particular, a comparable model configuration has been evaluated previously [*Dewitte et al.*, 2007; *Mosquera-Vásquez et al.*, 2013], which indicated that the model simulates realistically the fundamental features relevant to the equatorial wave dynamics at interannual timescales, including the mean temperature vertical structure. Despite the increased vertical resolution of the present version of the model compared to the version used in *Mosquera-Vásquez et al.* [2013], the realism of the mean thermocline (Figure 2c) is comparable, with a bias that consists in a weaker zonal and vertical gradient in the central equatorial Pacific than the observations. The interannual variability simulated by the model is rather realistic (Figure 2a, Tables 1 and 2). Regarding intraseasonal variability (Figure 2b), the realism of the model is reduced compared to interannual timescales, with still a fair agreement with observations. Since the ISKw activity is modulated at seasonal [*Illig et al.*, 2014] and interannual [*Dewitte et al.*, 2008] timescales, the validation of intraseasonal variability over the relative long record used here is a rather stringent test. The dispersion of the annual correlation is indicated in Figure 2b that shows that the correlation can reach up to 0.7 in the western Pacific for some specific periods. The most realistic period is 2004–2008, with 1996–1998 being the period with the lowest skill (not shown). Such limitation should be kept in mind for the interpretation of the results, considering that T323 is used as a diagnostic tool for the interpretation of the results derived from TAO.

The model outputs are further used to derive an estimate of the equatorial waves (sum of the first three baroclinic modes) based on a modal decomposition of the variability (pressure and zonal current), which is not possible to estimate from the available observations. The modal decomposition consists in deriving the vertical modes from the zonally slow-varying stratification over which pressure and zonal current anomalies are projected. This provides the baroclinic mode contribution to sea level and zonal current anomalies which are then projected onto the theoretical Kelvin and Rossby wave structures to derive the wave coefficients. The method is similar to *Dewitte et al.* [1999] and has been shown to extract the salient features of the equatorial waves [*Mosquera-Vásquez et al.*, 2013], including the effect of the zonally varying stratification, which is of major interest in this paper (see section 3.2).

### 2.4. Linear Ocean Model (LOM)

A simple Linear Ocean Model (hereafter referred to as LOM) for the tropical Pacific is used to interpret the characteristics of the ISKw in the equatorial Pacific as estimated in the OGCM T323 simulation. The linear model was used previously in *Mosquera* [2009]. It consists in one active layer with a linear friction of time decay τ. Note that the value of τ can varies from 6 to 30 months depending on the studies [*Picaut et al.*, 1993; *Dewitte et al.*, 1999] which reflects that dissipation processes may be frequency dependent and/or that a linear friction is not perfectly adequate to simulate wave dissipation. In this study, we will also use a linear friction to test to which extent it is adequate for simulating wave dissipation evidenced in the OGCM. Three experiments are carried out that differ either from the values used for friction or the structure of the thermocline: LOM-CR (control run) is the experiment that uses a constant friction of $(24 \text{ month})^{-1}$, while LOM-Rx uses a zonally varying time decay for friction, both experiments having a constant depth thermocline (H = 150 m). LOM-Hx is the experiment in which a zonally varying thermocline is used (derived from *Levitus and Boyer* [1994] data) along with a constant linear friction of $(24 \text{ month})^{-1}$.

Table 2. Correlation and RMS Difference of the Zonal Current Anomalies Averaged in the First 55 m Between T323 and TAO (1993–2010) at Five Mooring Locations

| Mooring Longitude	147°E	165°E	170°W	140°W	110°W
Mean correlation	0.8	0.84	0.67	0.5	0.64
Mean RMS difference (cm s^{-1})	14.7	14.8	17.3	20.1	21.4

Consistently with the T323 simulation, LOM is forced with wind stress anomalies derived from ERA-Interim data. Note that we also used wind stress from the NCEP/NCAR reanalysis and the results presented here are similar for both surface forcings. For consistency with the T323 outputs, only the results of the linear model with forcing from ERA-Interim fluxes are presented here.
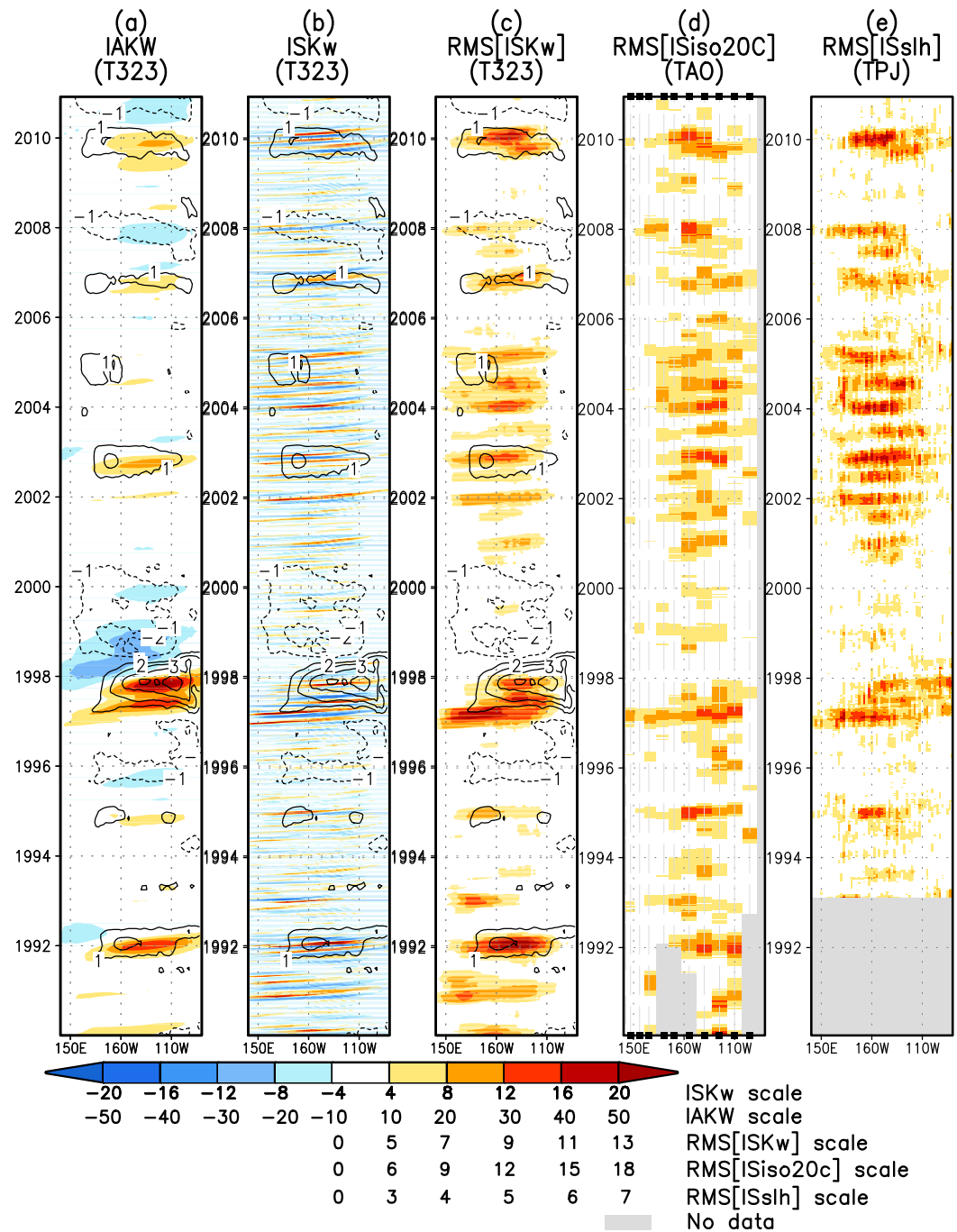
Figure 3. Time evolution of (a) interannual and (b) intraseasonal Kelvin wave contribution to thermocline depth (sum of the first three baroclinic modes) along the equator from T323. (c) Three month running RMS of the ISKw from T323, (d) TAO intraseasonal thermocline (20°C isotherm) depth anomalies, and (e) TPJ intraseasonnal sea level anomalies. Units are in meters, except in Figure 3e which is in centimeters. The contours in Figures 3a, 3b, and 3c indicate the interannual SST anomalies for T323 that is used to compare the maximum Kelvin wave activity with El Niño event along the Equatorial Pacific. Filled squares on the x axis in Figure 3d indicate the position of the TAO mooring buoys and the gray shading in Figures 3d and 3e corresponds to periods and locations when observations are not available.

3. Intraseasonal Kelvin Wave Activity

As a first step, we evaluate the contribution of the Interannual Kelvin wave (IAKw) and ISKw to the variability of thermocline depth along the equator, stressing on the distinct characteristics of the two types of El Niño events (Figure 3). The Kelvin wave anomalies consist here in the summed-up contribution of the first three baroclinic modes to the thermocline depth anomalies. The visual inspection of Figure 3a reveals clearly that
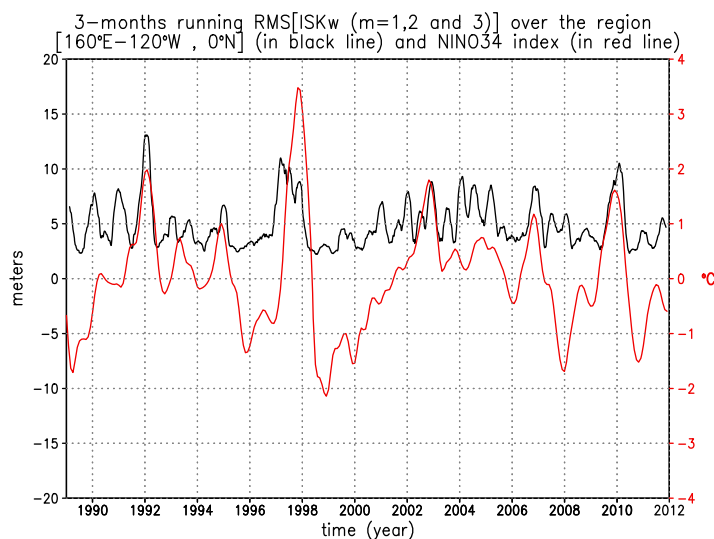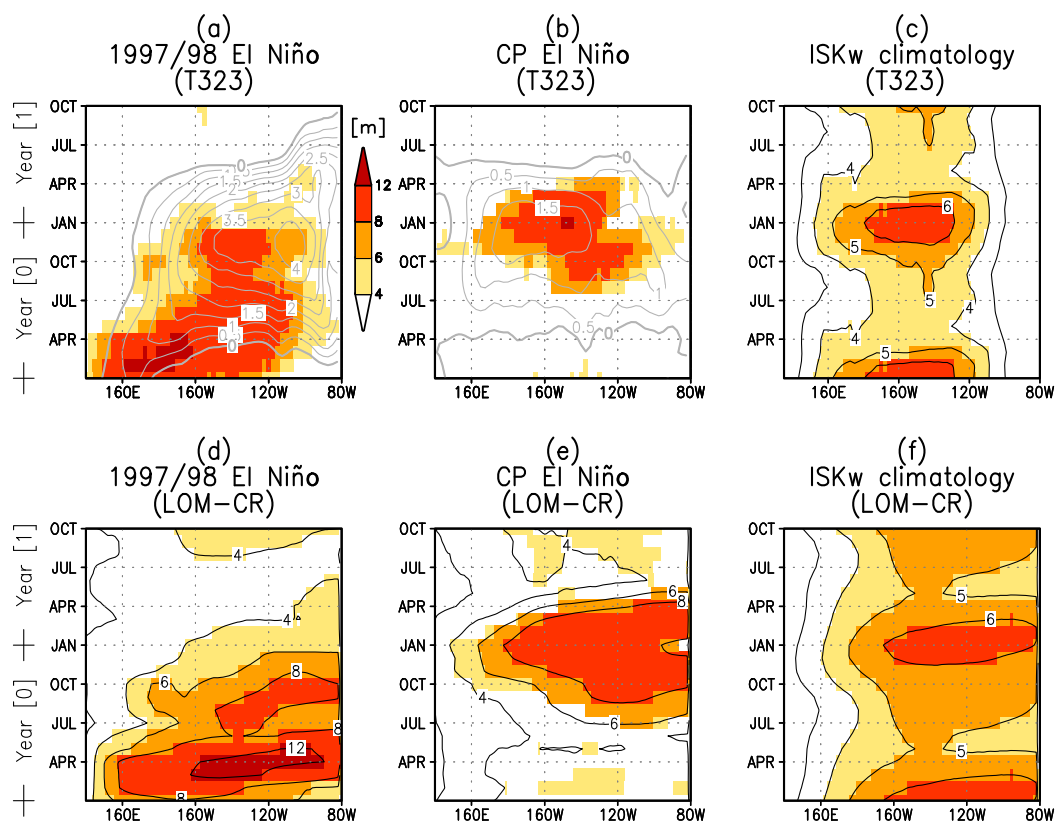
Figure 4. Time evolution of the 3 month running RMS of the (left scale) ISKw contribution to thermocline depth (sum of the first three baroclinic modes), averaged over the region [160°E–120°W; 0°N] (black line in meters), and (right scale) of the NINO343.4 index (red line in °C).

the CP El Niño events are associated with a relatively weak IAKw amplitude compared to the eastern Pacific 1997/1998 El Niño. The ratio of the peak amplitude of the IAKw between the 1997/1998 El Niño and the CP El Niño composite amplitude reaches 3. On the other hand, the inspection of the ISKw (Figure 3b) does not reveal any distinguishable differences in terms of amplitude between events. This is further illustrated in Figure 3c that shows the 3 month running RMS of the ISKw for T323. Peak in the ISKw activity is found for the periods 1991–1992, 1997–1999, 2002–2003, 2007–2008, and 2009–2010, which coincides with warming

and cooling events at intraseasonal timescale (Figure 3b). Figure 3c thus indicates that the magnitude of the ISKw activity is comparable between events, which is also evidenced in the in situ (Figure 3d) and altimetric (Figure 3e) data.

The time series of the T323 ISKw activity (3 month running RMS) averaged over the region (160°E–120°W; 0°) are displayed in Figure 4 along with the Niño 3.4 SST index (NINO34 (150°E–150°W; 5°S–5°N)), which indicates that the ISKw activity does not present the large positive asymmetry of the NINO34 index. In order to delineate the relative role of CP and EP El Niño events, we use the C and E indices obtained from the EOF analysis of SST in the tropical Pacific (see *Takahashi et al.*, [2011], for details). The ISKw activity index of Figure 4 correlates (with the maximum value at lag = 0) more to the C index (c = 0.5) than to the E index (c = 0.2), suggesting that ISKw activity is tightly linked to CP El Niño events during their peak phase. This is further illustrated by the composite evolution of the ISKw activity during CP El Niño events comparing to the ISKw variance during the 1997/1998 El Niño (Figure 5). This figure indicates that the ISKw activity during CP El Niño peaks in D(0)JF(+1), similar to interannual SST anomalies, whereas for the 1997/1998 El Niño, the peak variance is found around March(0), which is consistent with former studies [*Hendon et al.*, 2007; *McPhaden et al.*, 2006]. During a strong eastern Pacific event, the western Pacific tends to cool at the mature phase suppressing convection over the Maritime Continent region, so that MJO convective events maintain less continuity from the Indian basin to the central Pacific [*Hendon et al.*, 2007], explaining the reduced ISKw activity. Figure 5 further reveals the apparent strong dissipation of the ISKw activity in the eastern Pacific (around 120°W). Such dissipation may result from the shallowing thermocline that induces a slower phase speed of the wave or from local wind forcing at intraseasonal timescales [*Shinoda et al.*, 2008]. As a consistency check, the lag correlation as a function of longitude for a reference point at 120°W for the model (ISKw) and at 125°W for the thermocline depth intraseasonal anomalies as derived from TAO data is estimated and the result is presented in Figure 6. The equivalent plot for the altimetric data is also provided. It indicates that there is a slight change in characteristics of the propagating variability (slower phase speed, lower coherency) around 120°W for thermocline anomalies of TAO and T323. An estimation based on the slope of the straight line fitted to the maximum correlation west and east of 120°W indicates that the phase speed changes from 2.2 (2.7) to 1.5 (1.2) m s^{-1} for TAO data (T323). Interestingly, the altimetric data do not evidence changes in phase propagation, which is related to the fact that there is a larger contribution of the gravest baroclinic modes to sea level anomalies than to thermocline fluctuations in the eastern equatorial Pacific. These changes in propagating characteristics east of 120°W are also distinguishable directly on the amplitude of the intraseasonal anomalies. This is illustrated in Figure 7 that displays the RMS of the ISKw at each longitude normalized by the RMS of the ISKw at 120°W. The significant decrease of the ISKw

Figure 5. Longitude-time diagram along the equator of the ISKw activity (ISKw 3 month running RMS) for (top plots) T323 and (bottom plots) LOM-CR: for the 1997/1998 (left plots) El Niño event, (center plots) the composite of CP El Niño events, and (right plots) the averaged seasonal cycle. Units are in meters. The year [0] on the time axis of Figures 5a, 5b, 5d, and 5e refers to the El Niño years, that is El Niño peaking around December of year [0]. The interannual T323 SST anomalies corresponding to the 1997/1998 El Niño and the CP El Niño events composite are overlaid in Figures 5a and 5b in gray contour (°C). The shading in Figures 5a, 5b, 5d, and 5e indicates where values are significant at the 95% level, whereas in Figures 5c and 5f it only corresponds to values larger than 4 m. Significance levels were estimated using the bootstrap method [*Efron*, 1982].

variance east of 120°W indicates that a strong dissipation is taking place there. Similar dissipation characteristics cannot be accounted for by the linear model unless a very strong friction is applied east of 120°W. As a consistency check, an experiment is carried out with the linear model, in which the time decay for friction is reduced to 2 months east of 120°W. This location corresponds to the maximum in zonal gradient of the thermocline (blue line in Figure 7). West of 120°W, the time decay remains equal to 24 months as in the control experiment (LOM-CR). This experiment is called LOM-Rx and the results for the RMS of intraseasonal thermocline depth anomalies are displayed as a green curve in Figure 7. Even with such a strong friction, the decrease in RMS of the thermocline anomalies east of 120°W is not as strong as in T323, suggesting that other processes than just a linear dissipation is at work. This will be investigated further in section 4.

As a consistency check of the former statements inferred from the model outputs, TAO data are further analyzed using EOF decomposition. CP El Niño years are selected (from June (0) to May (+1)) and EOF analysis is carried out on the subsurface temperature intraseasonal anomalies of the first 300 m along the equator. The results are compared to the EOF analysis carried out for the EP El Niño event (June 1997 to May 1998). For both types of El Niño events, the result consists in two dominant modes exhibiting comparable explained variance, with associated time series phase-lagged by a quarter of period (not shown), indicating that the modes can be paired and corresponds to the eastward propagating variability associated with the ISKw along the thermocline (Figure 8). The second mode of the CP years is equivalent to a tilt mode of the thermocline, i.e., with a pattern consisting in a zonal seesaw with a node around 150°W. It has been verified that the associated time series are significantly correlated to the zonal wind stress anomalies at 165°E (maximum correlation of 0.43 for the wind stress ahead of the PC time series by 12 days) which indicates that this mode responds
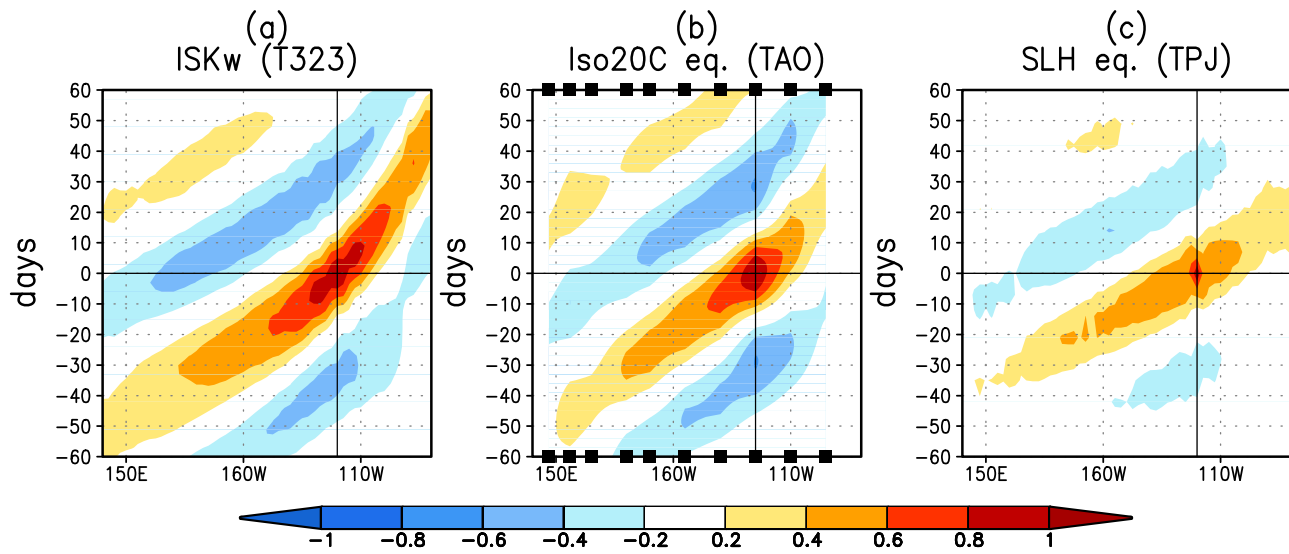
**Figure 6.** Lagged-correlation (from −60 to +60 days) along the equatorial line for a reference point equal or near to 120°W for (a) ISKw from T323, (b) intraseasonal thermocline depth anomalies from TAO, and (c) intraseasonal sea level anomalies from TPJ. The vertical thin line in Figures 6a and 6c indicates the longitude of 120°W (reference point) meanwhile in Figure 6b it is 125°W. The squares on the longitude axis (Figure 6b) indicate the positions of the TAO mooring buoys.

relatively rapidly to the wind stress forcing. On the other hand, the first mode has a pattern with an approximate zonal wave number of 2, which reflects the propagation nature of the paired EOF modes. Interestingly, the dominant EOF modes for CP El Niño years exhibit an overall much larger loading in the central Pacific than during the 1997 El Niño years. During the latter, the intraseasonal variability peaks in the eastern Pacific at a depth that corresponds to the mean thermocline depth over this period (see orange dashed line in Figures 8b and 8d) and the paired modes are indicative of eastward propagation as far as the eastern boundary. In contrast, during the CP El Niño years, the variability peaks along (or just below) the mean thermocline and east of ∼120°W, it exhibits a very weak amplitude of the paired modes, evidencing the strong dissipation taking place east of 120°W.
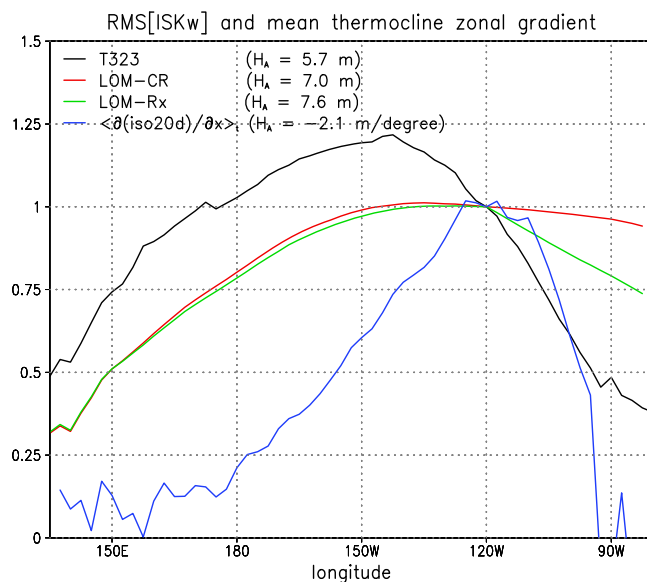
Figure 7. RMS of ISKw for T323 (black line), LOM-CR (red line), and LOM-Rx (green line). The blue line shows the temporal mean of the zonal gradient of the 20°C isotherm (thermocline) depth from T323. Values are adimensionalized by their respective values at 120°W (indicated in the upper left corner as H_A).

Further, the amplitude of the EOF time series is estimated as $\sqrt{PC_1(t)^2 + PC_2(t)^2}$ where $PC_n(t)_{n=[1,2]}$ are the normalized time series associated with the EOF modes, and monthly mean climatologies are derived, which indicates the privileged seasons for intraseasonal activity. The results are presented in Figure 8e. They indicate that the peak season for intraseasonal variability along the thermocline during CP El Niño years is December to February, which is consistent with the model results (Figure 5). The range of values associated with the dispersion of the six CP El Niño years (shading in Figure 8e) suggests that such feature is significantly different from the
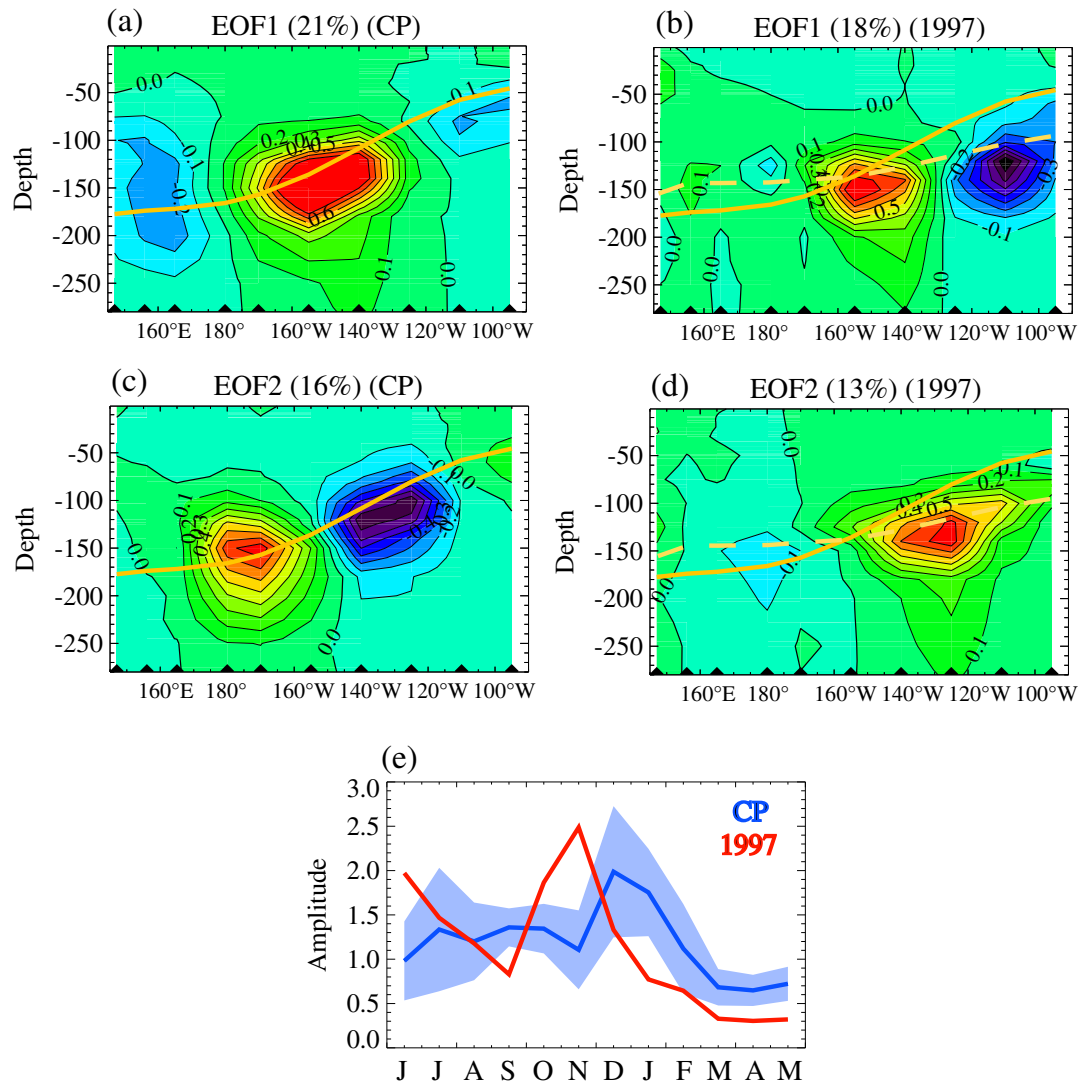
Figure 8. EOF decomposition of (a, c) observed (TAO) subsurface temperature intraseasonal anomalies along the equator over the years of CP El Niño events and (b, d) of the 1997/1998 El Niño event. First (second) EOF patterns in the first 300 m are displayed in the top (center) plots. Years are considered from June (0) to May (+1). The orange thick plain (dashed) line indicates the mean thermocline depth over the 2000–2011 period (June 1997 to May 1998). The black triangles on the longitude axis indicate the positions of the TAO mooring buoys. (e) Monthly mean climatology of the amplitude of the intraseasonal mode defined as $\sqrt{PC_1(t)^2 + PC_2(t)^2}$ where $PC_n(t)_{n=[1,2]}$ are the normalized time series associated with the EOF modes for (blue line) CP El Niño years. The shading indicates the dispersion over the six CP El Niño years (i.e., + and − the variance among the CP years). The red line corresponds to the monthly mean of the amplitude of the intraseasonal mode for the 1997/1998 El Niño event, i.e., during the period June 1997 to May 1998.

1997 El Niño year during which the intraseasonal variability peaks around November and then decreases sharply, maintaining a low amplitude until May 1998.

Both model results and observations suggest that dissipation processes take place around 120°W during CP El Niño years. The next section investigates to which extent such feature can be interpreted in terms of modal dispersion that is the process of the scattering of energy between baroclinic modes when the wave crosses a region with distinct density [*Busalacchi and Cane*, 1988; *Harrison and Giese*, 1991].

4. Wave Dispersion in the Eastern Pacific

4.1. Rossby Wave Activity and Role of Wind Forcing

To further get insights on the processes taking place in the eastern equatorial Pacific, we display the Intra-Seasonal Rossby wave (ISRw) variance (3 month running RMS) (Figure 9a) as derived from the modal
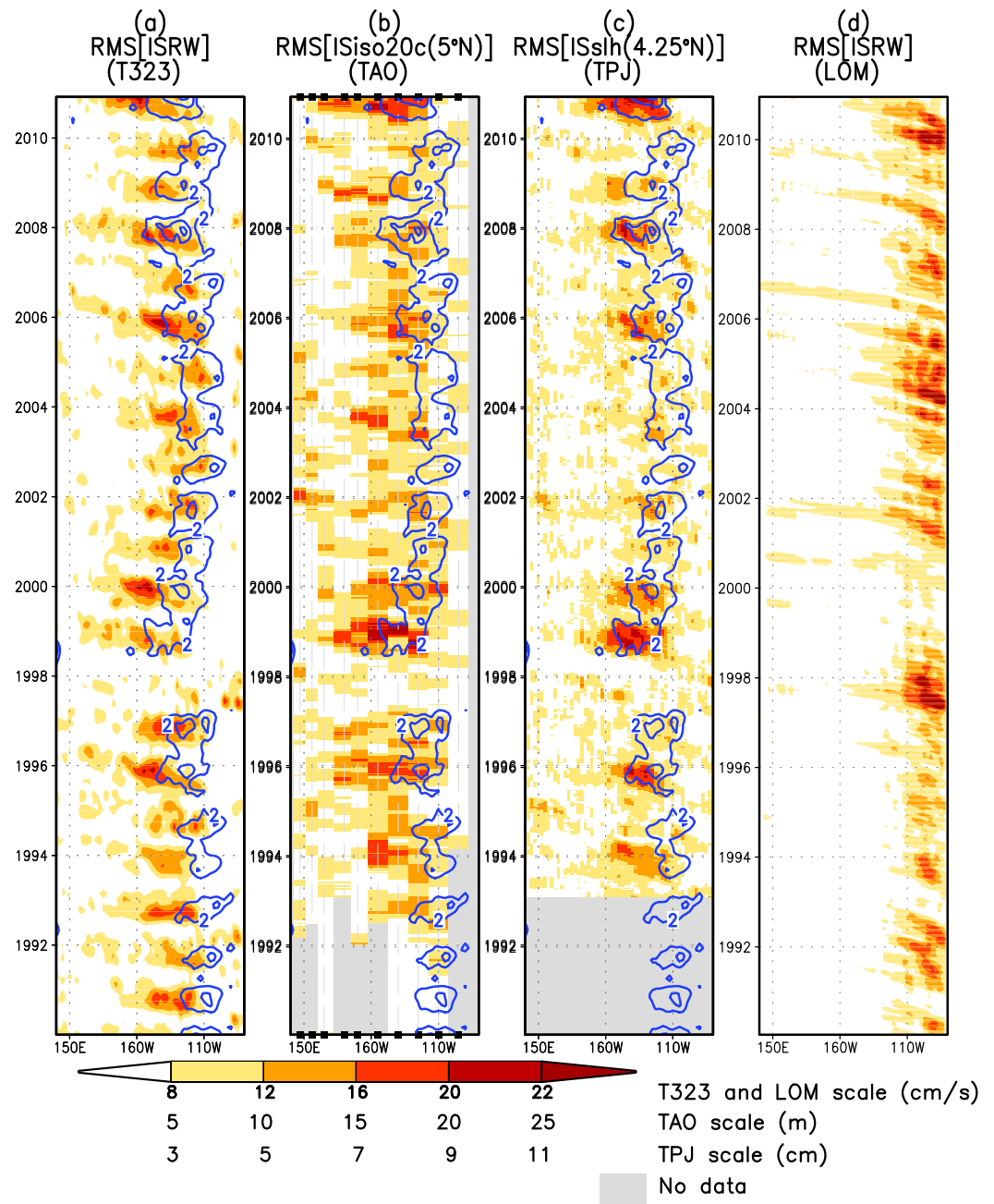
Figure 9. Time evolution of the 3 month running RMS of (a) the ISRw (equivalent zonal current, first-meridional mode, cm s^{-1}) from T323 along the equatorial line and (b) the intraseasonal thermocline (20°C isotherm) depth anomalies (in m) from TAO at 5°N. (c) Same as (b) but for TPJ sea level anomalies at 4.25°N (in cm). (d) Same as (a) but for LOM-Hx. Filled squares indicate the position of the TAO mooring buoys and the gray shading where data are not available. The blue contours indicate the zonal gradient of the thermocline from T323 in absolute value. Units are in m/°. Only gradients larger than 2 m/° are shown.

decomposition of the T323 simulation. The Rossby wave consists here in the first three baroclinic mode summed-up contribution of the first-meridional Rossby modes in term of zonal current and can be compared to the variance of the observed sea level anomalies or thermocline anomalies at 5°S (i.e., where first-meridional Rossby wave structure of the first baroclinic mode is maximum) (Figures 9b and 9c). Figures 9a–9c evidence westward propagating variability for T323, TAO, and TPJ data. Strikingly the propagation is only clearly observable west of ~120°W from which the ISRw activity seems to originate. The region where the ISRw variance originates coincides with the location of the maximum zonal gradient of the thermocline depth (blue contour overplotted in Figures 9a–9c) suggesting that the ISRw results either from the
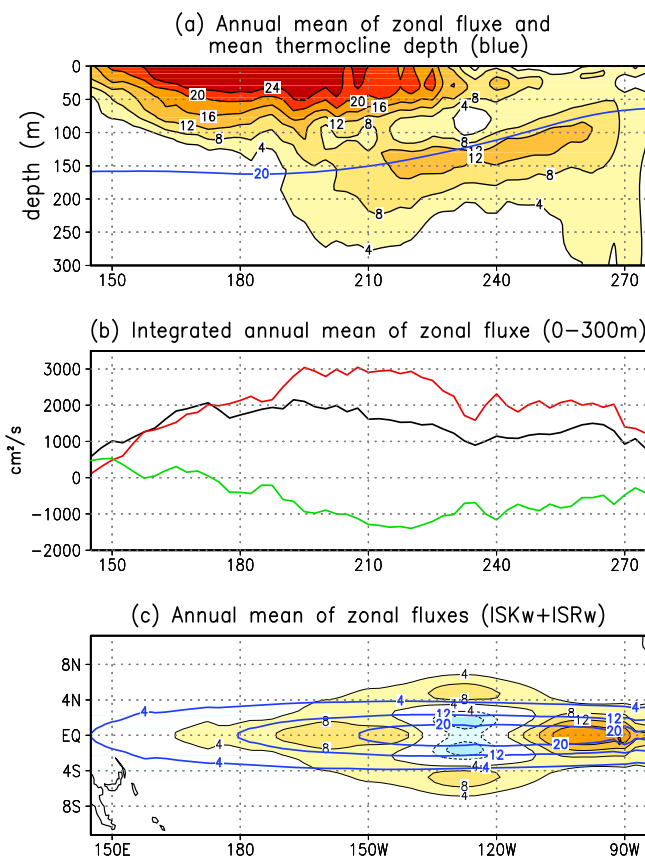
Figure 10. Annual mean of the zonal energy flux for (a) the depth-integrated (from bottom to surface) zonal flux for the ISKw and ISRw, (b) depth-integrated (0–300 m) zonal flux, and (c) the total flux as a function of longitude and latitude. In Figure 10b, the black line represents the total zonal flux, the solid red line is the sum of the first three baroclinic modes, and the green line is the residual (see text). In Figure 10c, the blue line indicates the mean thermocline depth. Units are in $m^2\,s^{-1}$ for Figures 10a and 10c, and $cm^2\,s^{-1}$ for Figure 10c.

reflection of the ISKw on the sharp zonal density front (see next section) or from wind forcing. As a consistency check, the ISRw is derived from the linear model control run (LOM-CR) and displayed in Figure 9d. It reveals that the ISRw cannot be accounted for by the wind stress forcing since the maximum of variability is confined to the far eastern Pacific in the linear model experiment indicating that the ISRw variability originates from the reflections of the ISKw at the eastern boundary. Noteworthy, the ISRw activity in 2001–2002 west of 120°W in T323 could be explained to some extent by the wind stress forcing consistently with the study by *Shinoda et al.* [2008]. The linear model is further used to test if ISRw can be modified by the zonally varying thermocline. The results indicate that, within a realistic range of values for the thermocline slope, the model does not simulate significant Kelvin wave reflection at the longitude where the thermocline gradient is maximum. A composite analysis of the ISKw and wind stress anomalies during CP El Niño years also revealed that an easterly wind stress event follows the peak phase of the main downwelling ISKw (not shown), which could have the potential to alter the downwelling ISKw in the eastern Pacific and contribute to the dissipation observed at 120°W. However, the easterly wind stress event is located slightly to the west of the previous westerly wind stress event and does not coincide with the crest of the downwelling ISKw, which rules out any role of the easterly wind stress event in dissipating the downwelling ISKw in the eastern Pacific. The linear model results confirm this interpretation (not shown). This indicates that the features observed in T323 cannot be accounted for by the linear model, and that the maximum variance in ISRw west of 120°W results from nonlinear processes.

4.2. Energy Scattering

The former analysis suggests that the energy of the ISKw is scattered near 120°W corresponding to the region where the largest zonal gradient in stratification (thermocline) is found. In order to evidence the dispersion, we estimate from T323 simulation, the zonal energy flux along the equator [*Eliassen and Palm*, 1960]. It consists in calculating the quantity $\langle u'(x, y=0, z, t) . p'(x, y=0, z, t)\rangle$, where ' denotes intraseasonal anomalies and the brackets stand for the temporal average performed over the CP El Niño years. This horizontal energy flux is displayed along the equator within the first 300 m between 140°W and 90°W (Figure 10a). It indicates that the zonal energy flux experiences an eastward change in vertical structure, with the energy concentrated in the upper layer (first 100 m) in the central-western Pacific (accounting for mixing associated with the local wind power) and just below the thermocline in the eastern Pacific (which cannot be accounted for the local winds). It was checked that energy flux is enhanced during CP El Niño years

compared to the mean energy flux calculated over the whole record with a comparable pattern (not shown). The change in vertical structure of the zonal energy flux from west to east is indicative of modal dispersion associated with the zonal gradient in mean thermocline. In order to quantify this, we consider the depth-integrated zonal energy flux within the first 300 m (ZF300). Assuming that u' and p' can be decomposed into an infinite sum of baroclinic modes such as $u' = \sum_{n=1}^{\infty} u_n F_n(z)$ and $p' = \sum_{n=1}^{\infty} p_n F_n(z)$, the 300 m depth-integrated zonal flux can write as follows:

$$ZF300 = \int_{-300}^{0} \langle u' \cdot p' \rangle dz = \sum_{n=1}^{3} \sum_{m=1}^{3} \langle u'_n \cdot p'_m \rangle \int_{-300}^{0} F_n(z) \cdot F_m(z) dz + R$$

Here $F_n(z)$ are the baroclinic mode functions that also depend on longitude [*Dewitte et al.*, 1999], and R is a residual accounting for the contribution of the high-order baroclinic modes. R therefore writes as follows:

$$R = \sum_{n=1}^{3} \sum_{m=4}^{\infty} \langle u'_n \cdot p'_m \rangle \int_{-300}^{0} F_n(z) \cdot F_m(z) dz + \sum_{n=4}^{\infty} \sum_{m=1}^{3} \langle u'_n \cdot p'_m \rangle \int_{-300}^{0} F_n(z) \cdot F_m(z) dz + \sum_{n=4}^{\infty} \sum_{m=4}^{\infty} \langle u'_n \cdot p'_m \rangle \int_{-300}^{0} F_n(z) \cdot F_m(z) dz$$

The term $\sum_{n=1}^{3} \sum_{m=1}^{3} \langle u'_n \cdot p'_m \rangle \int_{-300}^{0} F_n(z) \cdot F_m(z) dz$ represents the zonal flux in the upper 300 m associated with the propagating waves, while R accounts for the energy flux associated with locally forced variability that can originate from either local wind forcing or mixing. Both terms implicitly include the effect of modal dispersion onto the zonal energy flux if any, and their zonal variability may be indicative of such a process. If there is no scattering of energy, change in energy flux is to be due to dissipation process if local wind forcing is weak, and therefore the flux should decrease eastward. Figure 10b shows the depth-integrated zonal flux along the equator for the aforementioned terms. Interestingly, the integrated zonal flux associated with the first three baroclinic mode (black curve) has a local minimum at ∼120°W, from which it increases eastward. Such increase can be interpreted in term of the larger trapping of zonal flux along the equator by the Kelvin wave due to the finer meridional scales (smaller phase speed) in the eastern Pacific, which is also evidenced in Figure 10c that shows the zonal flux associated with the Kelvin and Rossby waves (first three baroclinic modes) integrated over the whole water column (i.e., $\sum_{n=1}^{3} \langle u'_n \cdot p'_n \rangle$ where only the contributions of the Kelvin and first to third meridional Rossby waves to (u'_n, p'_n) are considered). Figure 10c shows that the zonal flux associated with the Kelvin wave is increased eastward due to the decrease in meridional scale of the Kelvin wave (resulting from the shallower thermocline). West of 120°W, the signature of the Rossby waves on the zonal flux is more prominent than east of 120°W, indicative of the partial reflection of the Kelvin waves into Rossby waves on the zonal front in stratification, consistently with results of Figure 9. The increase in the zonal flux east of 120°W also results from a redistribution of energy between baroclinic modes toward the higher-order modes as evidenced by the slight increase of the residual term (R) east of 120°W (green curve in Figure 10b).

Another indication of modal dispersion is provided by the spectral analysis of the thermocline depth fluctuations west and east of the density front at ∼120°W, which can be estimated from the TAO data. The variations of thermocline depth are estimated from the EOF analysis of intraseasonal temperature anomalies in the vicinity of the mean thermocline in the central Pacific (i.e., at 180°, 170°W, 155°W between 120 and 215 m) and the eastern Pacific (i.e., at 110°W, 95°W between 30 and 80 m). Only the six CP El Niño years are considered. We retain the first two modes which summed-up contribution explains more than 79% of the explained variance. A wavelet decomposition of the EOF time series is then performed. Since there is a marked seasonal dependence of the intraseasonal variability, the climatological wavelet spectrum is estimated which consists in calculating the climatology of the wavelet power coefficient at each frequencies. Wavelet power was first normalized following equation (14) of *Torrence and Compo* [1998] in order to compare the magnitude of the wavelet power at different frequencies, following the method introduced in *Goubanova et al.* [2013]. The results are presented in Figure 11. Figure 11 shows that there is a significant change in the seasonality of the intraseasonal variability of the thermocline depth fluctuations: intraseasonal variability peak in Austral summer west of 120°W, whereas it tends to peak in Austral winter east of 120°W. In addition, there is a tendency for a broadening of the global wavelet spectrum from west to east, in particular toward lower frequencies. Since the wind forcing is weak in the eastern Pacific at intraseasonal
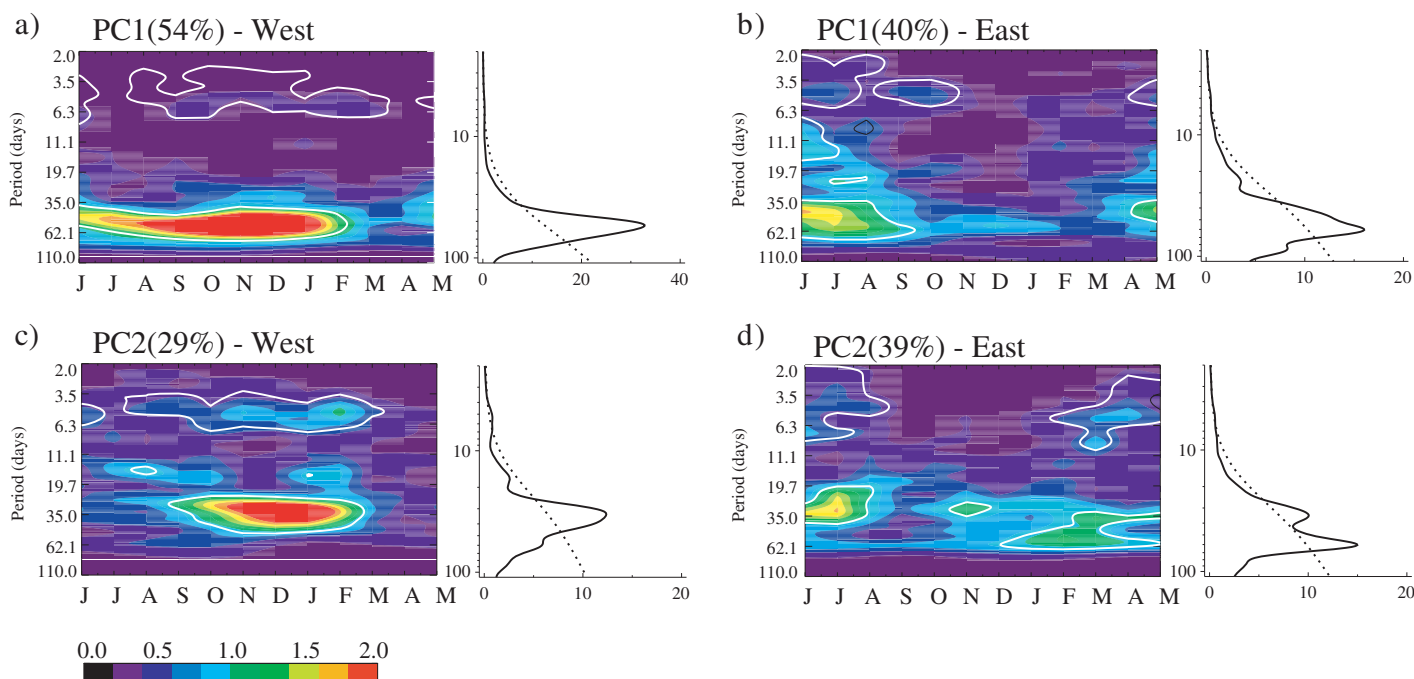
Figure 11. Spectral analysis of the intraseasonal thermocline depth anomalies from TAO in the (a, c) central Pacific (180°, 170°W, 155°W) and the (b, d) eastern Pacific (110°W, 95°W): climatological normalized power wavelet (Morlet) spectrum and global wavelet spectrum of the time series associated with the Figures 11a and 11b first and Figures 11c and 11d second EOF modes of intraseasonal temperature anomalies in the vicinity of the mean thermocline. The climatological normalized power wavelet spectrum consists in a wavelet decomposition of the time series followed by a calculation of the climatology of the Wavelet Power coefficient at each frequencies. Wavelet Power was first normalized following equation (14) of *Torrence and Compo* [1998] in order to compare the magnitude of the wavelet power at different frequencies. Scale is indicated on the bottom of Figure 11c. Unit is adimensionalized (but scaled by 10^{-1}) since EOF time series are normalized. The percentage of explained variance of the EOF modes is indicated on top of each plot. The dashed black line in the global wavelet spectrum and the white contour in the climatological wavelet spectrum indicate the 95% confidence level estimated from a red noise (Markov model).

timescales, the change in the spectral characteristics of the thermocline fluctuations from west to east is due to changes in the background state, inducing to modal dispersion.

5. Discussion and Conclusions

The characteristics of the intraseasonal Kelvin wave in the Pacific are examined based on observations (TAO data and altimetry) and an OGCM simulation covering the period 1989–2011. We show that the expression of the intraseasonal temperature variability is dominant in the vicinity of the thermocline (and not at the surface), which is associated with the contribution of the first three baroclinic mode Kelvin waves to the thermocline anomalies. It is then evidenced that the CP El Niño events are associated with an increase in intraseasonal equatorial Kelvin activity compared to neutral years. The peak variance takes place during the mature phase of the CP El Niño events which is in contrast with the extreme 1997/1998 El Niño event for which the peak variance takes place 5–6 months earlier. Whereas the peak variance of the intraseasonal Kelvin wave during CP El Niño event is wind-forced in the central Pacific as inferred from the linear model simulations performed in this study, the Kelvin wave in the eastern Pacific experiences a drastic change in its characteristics, which cannot be accounted for by just a linear dissipation in the linear model and wind stress forcing. It is shown that the region from which the Kelvin wave starts strongly dissipating coincides with the location of the maximum thermocline zonal gradient (~120°W). This region also corresponds to the location where intraseasonal Rossby waves originate, which cannot be accounted for by a linear model, suggesting scattering of energy of the Kelvin wave as it propagates eastward and partial reflections on the density front. An analysis of the zonal flux in the OGCM is consistent with this interpretation revealing in particular a sharp change in its vertical structure near 120°W and an increase in the zonal flux associated with the high-order baroclinic modes in the far eastern Pacific. The eastward change in spectral characteristics of the thermocline fluctuations from TAO data is also consistent with the process of modal dispersion.

Our results may have implications for the understanding of the modulation of ENSO; in particular, the increased occurrence of CP El Niño events over the recent decades [*Yeh et al.*, 2009; *Lee and McPhaden*, 2010]. In the light of our results, it may be hypothesized that an increase in the zonal contrast of the thermocline is favorable for modal dispersion of the intraseasonal Kelvin wave preventing its free propagation in the far eastern Pacific where it could trigger a local wind response (local Bjerknes feedback) through its impact on SST via the strong thermocline feedback there. Interestingly since the late of the 1990s, the tropical Pacific has entered a La Niña-like state [cf. *Xiang et al.*, 2013] that is associated with a slightly steeper thermocline. A Coupled General Circulation Model (CGCM) that simulates a decadal variability in the ratio of occurrence of CP El Niño and EP El Niño events indicates that the latter is associated with a decadal mode in the thermocline zonal gradient across the equatorial Pacific [*Choi et al.*, 2011] with the periods of increased occurrence of CP El Niño characterized by a steeper mean thermocline. Such feature has also been suggested from observations for the transition in mean state of the 2000s [*McPhaden et al.*, 2011]. The intraseasonal Kelvin wave could thus be "trapped" in the central Pacific during periods when the zonal contrast in stratification is increased [see *Dewitte et al.*, 2012b, Figure 8] for the estimate of the Kelvin wave in the GFDL_CM2.1 model for CP El Niño events). Note that this is consistent with the study by *Hu et al.* [2013] which suggests that the combination of a steeper thermocline slope with stronger surface trade winds has hampered the eastward migration of the warm waters along the equatorial Pacific since 2000, favoring the occurrence of CP El Niño events. The steeper thermocline leads to a strong zonal contrast in stratification which can alter the Intraseasonal Kelvin wave characteristics through modal dispersion. This is in contrast with recent studies [*Xiang et al.*, 2013; *Dommenget et al.*, 2012] that rather suggest a nonlinear atmospheric process for explaining the predominance of CP El Niño events under a La Niña-like mean state, which calls for further study. The latter could be based on the experimentation with a tropical Pacific OCGM allowing the analysis of an explicit heat budget to diagnose mixing and diffusive processes. In particular, it could be interesting to assess if there is a threshold associated with the amplitude of the equatorial Kelvin wave from which vertical diffusivity increases sharply, mixing baroclinic modes, and preventing the Kelvin wave to propagate freely. There is also the possibility that the intraseasonal Kelvin wave propagates vertically along steep WKB ray paths from its forcing region at the surface in the central Pacific and encounters the stratification front associated with the mean thermocline further east. There is indication of such a process in the OGCM used here (not shown) suggesting that scattering of energy in the east might be taking place both in the zonal and vertical directions. Further study will be dedicated to the investigation of such process.

References

Ashok, K., S. K. Behera, S. A. Rao, H. Weng, and T. Yamagata (2007), El Niño Modoki and its possible teleconnection, *J. Geophys. Res.*, *112*, C11007, doi:10.1029/2006JC003798.

Bergman, J. W., H. H. Hendon, and K. M. Weickmann (2001), Intraseasonal air-sea interactions at the onset of El Niño, *J. Clim.*, *14*, 1702–1719.

Busalacchi, A. J., and M. A. Cane (1988), The effect of varying stratification on low-frequency equatorial motions, *J. Phys. Oceanogr.*, *18*(6), 801–812.

Capotondi, A., et al. (2014), Understanding ENSO diversity, *Bull. Amer. Met. Soc.*, in press.

Choi, J., S.-I. An, J.-S. Kug, and S.-W. Yeh (2011), The role of mean state on changes in El Niño's flavor, *Clim. Dyn.*, *37*, 1205–1215, doi:10.1007/s00382-010-0912-1.

Cravatte, S., J. Picaut, and G. Eldin (2003), First and second baroclinic Kelvin modes in the equatorial Pacific at intraseasonal timescales, *J. Geophys. Res.*, *108*(C8), 3266, doi:10.1029/2002JC001511.

Dewitte, B., G. Reverdin, and C. Maes (1999), Vertical structure of an OGCM simulation of the equatorial Pacific Ocean in 1985–1994, *J. Phys. Oceanogr.*, *29*, 1542–1570.

Dewitte, B., S. Illig, L. Parent, Y. duPenhoat, L. Gourdeau, and J. Verron (2003), Tropical Pacific baroclinic mode contribution and associated long waves for the 1994–1999 period from an assimilation experiment with altimetric data, *J. Geophys. Res.*, *108*(C4), 3121, doi:10.1029/2002JC001362.

Dewitte, B., S.-W. Yeh, B.-K. Moon, C. Cibot, and L. Terray (2007), Rectification of the ENSO variability by interdecadal changes in the equatorial background mean state in a CGCM simulation, *J. Clim.*, *20*, 2002–2021, doi:10.1175/JCLI4110.1.

Dewitte, B., S. Purca, S. Illig, L. Renault, and B. Giese (2008), Low frequency modulation of the intraseasonal equatorial Kelvin wave activity in the Pacific ocean from SODA: 1958–2001, *J. Clim.*, *21*, 6060–6069.

Dewitte, B., S. Thual, S.-W. Yeh, S.-I. An, B.-K. Moon and B. Giese (2009), Low frequency variability of temperature in the vicinity of the equatorial thermocline in SODA: Role of equatorial wave dynamics and ENSO asymmetry, *J. Climate*, *22*, 5783–5795.

Dewitte, B., S.-W. Yeh, and S. Thual (2012a), Reinterpreting the thermocline feedback in the central-western Pacific and its relationship with the ENSO modulation, *Clim. Dyn.*, *41*(3–4), 819–830, doi:10.1007/s00382-012-1504-z.

Dewitte, B., J. Choi, S.-I. An, and S. Thual (2012b), Vertical structure variability and equatorial waves during central Pacific and eastern Pacific El Niño in a coupled general circulation model, *Clim. Dyn.*, *38*(11–12), 2275–2289, doi:10.1007/s00382-011-1215-x.

Dommenget, D., T. Bayr, and C. Frauen (2012), Analysis of the non-linearity in the pattern and time evolution of El Niño Southern Oscillation, *Clim. Dyn.*, *40*, 2825–2847.

Ducet, N., P. Y. Le Traon, and G. Reverdin (2000), Global high resolution mapping of ocean circulation from TOPEX/POSEIDON and ERS-1/2, *J. Geophys. Res.*, *105*, 19,477–19,498.

Efron, B. (Ed.) (1982), *The Jackknife, the Bootstrap, and Other Resampling Plans, CBMSNSF Monogr. 38*, 92 pp., Soc. for Ind. and Appl. Math, doi:10.1137/1.9781611970319.

Eisenman, I., L. Yu, and E. Tziperman (2005), Westerly wind bursts: ENSO's tail rather than the dog?, *J. Clim.*, *18*(24), 5224–5238, doi:10.1175/JCLI3588.1.

Eliassen, A., and E. Palm (1960), On the transfer of energy in stationary mountain waves, *Geofys. Publ.*, *22*(3), 1–23.

Fu, L.-L., E. J. Christensen, C. A. Yamarone Jr., M. Lefebvre, Y. Menard, M. Dorrer, and P. Escudier (1994), Topex/Poseidon mission overview, *J. Geophys. Res.*, *99*, 24,369–24,381.

Giese, B. S., and D. E. Harrison (1991), Eastern equatorial Pacific response to three composite westerly wind types, *J. Geophys. Res.*, *96*, 3239–3248.

Giese, B. S., and S. Ray (2011), El Niño variability in simple ocean data assimilation (SODA), 1871–2008, *J. Geophys. Res.*, *116*, C02024, doi:10.1029/2010JC006695.

Goubanova, K., S. Illig, E. Machu, V. Garçon, and B. Dewitte (2013), SST subseasonal variability in the central Benguela upwelling system as inferred from satellite observations (1999–2009), *J. Geophys. Res. Oceans*, *118*, 4092–4110, doi:10.1002/jgrc.20287.

Gushchina, D., and B. Dewitte (2012), Intraseasonal tropical atmospheric variability associated to the two flavors of El Niño, *Mon. Weather Rev.*, *140*(11), 3669–3681.

Hayes, S. P., P. Chang, and M. J. McPhaden (1991), Variability of the seasurface temperature in the eastern equatorial Pacific during 1986–88, *J. Geophys. Res.*, *96*, 10,553–10,566.

Hendon, H. H., B. Liebmann, and J. D. Glick (1998), Oceanic Kelvin waves and the Madden-Julian oscillation, *J. Atmos. Sci.*, *55*, 88–101.

Hendon, H. H., M. C. Wheeler, and C. Zhang (2007), Seasonal dependence of the MJO–ENSO relationship, *J. Clim.*, *20*, 531–543, doi:10.1175/JCLI4003.1.

Hu, Z.-Z., A. Kumar, B. Jha, W. Wang, B. Huang, and B. Huang (2012), An analysis of warm pool and cold tongue El Niños: Air-sea coupling processes, global influences, and recent trends, *Clim. Dyn.*, *38*(9–10), 2017–2035, doi:10.1007/s00382-011-1224-9.

Hu, Z.-Z., A. Kumar, H.-L. Ren, H. Wang, M. L'Heureux, and F.-F. Jin (2013), Weakened interannual variability in the tropical Pacific Ocean since 2000, *J. Clim.*, *26*(8), 2601–2613, doi:10.1175/JCLI-D-12-00265.1.

Illig, S., B. Dewitte, K. Goubanova, G. Cambon, J. Boucharel, F. Monetti, C. Romero, S. Purca, and R. Flores (2014), Forcing mechanisms of intraseasonal SST variability off Central Peru in 2000–2008, *J. Geophys. Res. Oceans*, *119*, 3548–3573, doi:10.1002/2013JC009779.

Jin, F.-F., L. Lin, A. Timmermann, and J. Zhao (2007), Ensemble-mean dynamics of the ENSO recharge oscillator under state-dependent stochastic forcing, *Geophys. Res. Lett.*, *34*, L03807, doi:10.1029/2006GL027372.

Johnson, N. C. (2013), How many ENSO flavors can we distinguish?, *J. Clim.*, *26*, 4816–4827, doi:10.1175/JCLI-D-12-00649.1.

Kao, H.-Y., and J.-Y. Yu (2009), Contrasting eastern-Pacific and central-Pacific types of ENSO, *J Clim.*, *22*, 615–632.

Kessler, W. S., and R. Kleeman (2000), Rectification of the Madden-Julian oscillation into the ENSO cycle, *J. Clim.*, *13*, 3560–3575.

Kessler, W. S., and M. J. McPhaden (1995a), The 1991–93 El Niño in the central Pacific, *Deep Sea Res., Part II, 42*, 295–333.

Kessler, W. S., and M. J. McPhaden (1995b), Oceanic equatorial waves and the 1991–93 El Niño, *J. Clim.*, *8*, 1757–1774.

Kessler, W. S., M. J. McPhaden, and K. M. Weickmann (1995), Forcing of intraseasonal Kelvin waves in the equatorial Pacific, *J. Geophys. Res.*, *100*, 10,613–10,631.

Kug, J.-S., F.-F. Jin, and S.-I. An (2009), Two types of El Niño events: Cold tongue El Niño and warm pool El Niño, *J. Clim.*, *22*, 1499–1515.

Lee, T., and M. J. McPhaden (2010), Increasing intensity of El Niño in the central-equatorial Pacific, *Geophys. Res. Lett.*, *37*, L14603, doi:10.1029/2010GL044007.

Lengaigne, M., E. Guilyardi, J. P. Boulanger, C. Menkes, P. Delecluse, P. Inness, J. Cole, and J. Slingo (2004), Triggering of El Niño by westerly wind events in a coupled general circulation model, *Clim. Dyn.*, *23*, 601–620.

Le Traon, P. Y., and F. Ogor (1998), ERS-1/2 orbit improvement using T/P: The 2 cm challenge, *J. Geophys. Res.*, *103*, 8045–8057.

Levitus, S., and T. P. Boyer (1994), World Ocean Atlas 1994 Volume 4: Temperature, in *NOAA Atlas NESDIS 4*, 117 pp., U.S. Dep. of Commer., Washington, D. C.

Lin, J. W. B., J. D. Neelin, and N. Zeng (2000), Maintenance of tropical intraseasonal variability: Impact of evaporation-wind feedback and midlatitude storms, *J. Atmos. Sci.*, *57*, 2793–2823.

Madden, R., and P. Julian (1972), Description of global-scale circulation cells in the tropics with a 40–50 day period, *J. Atmos. Sci.*, *29*, 1109–1123.

Madec, G., P. Delecluse, M. Imbard, and C. Levy (1998), *OPA 8.1 Ocean General Circulation Model Reference Manual, Nodes du pole de modélisation 11*, 91 pp., Inst. Pierre Simon Laplace, France.

McPhaden, M. J. (1999), Genesis and evolution of the 1997–98 El Niño, *Science*, *283*, 950–954.

McPhaden, M. J. (2002), Mixed layer temperature balance on intraseasonal time scales in the equatorial Pacific Ocean, *J. Clim.*, *15*(18), 2632–2647.

McPhaden, M. J. (2012), A 21st century shift in the relationship between ENSO SST and warm water volume anomalies, *Geophys. Res. Lett.*, *39*, L09706, doi:10.1029/2012GL051826.

McPhaden, M. J., and B. A. Taft (1988), On the dynamics of seasonal and intraseasonal variability in the eastern equatorial Pacific, *J. Phys. Oceanogr.*, *18*, 1713–1732.

McPhaden, M. J., et al. (1998), The Tropical Ocean-Global Atmosphere (TOGA) observing system: A decade of progress, *J. Geophys. Res.*, *103*, 14,169–14,240.

McPhaden, M. J., X. Zhang, H. H. Hendon, and M. C. Wheeler (2006), Large scale dynamics and MJO forcing of ENSO variability, *Geophys. Res. Lett.*, *33*, L16702, doi:10.1029/2006GL026786.

McPhaden, M. J., T. Lee, and D. McClurg (2011), El Niño and its relationship to changing background conditions in the tropical Pacific, *Geophys. Res. Lett.*, *38*, L15709, doi:10.1029/2011GL048275.

Mosquera, K. (2009), Variabilidad intra-estacional de la Onda de Kelvin Ecuatorial en el Pacífico (2000–2007): Simulación numérica y datos observados, MS thesis, 76 pp., Univ. Nacl. Mayor de San Marcos, Lima, Perú.

Mosquera-Vásquez, K., B. Dewitte, S. Illig, K. Takahashi, and G. Garric (2013), The 2002/03 El Niño: Equatorial wave sequence and their impact on sea surface temperature, *J. Geophys. Res.*, *118*, doi:10.1029/2012JC008551.

Picaut, J., C. Menkes, J.-P. Boulanger, and Y. duPenhoat (1993), Dissipation in the Pacific Equatorial long wave model, *TOGA Notes*, *10*, 11–15.

Ramos, M., B. Dewitte, O. Pizarro, and G. Garric (2008), Vertical propagation of the extra-tropical Rossby wave during the 1997/98 El Niño off the west coast of South-America in a medium-resolution OGCM simulation, *J. Geophys. Res.*, *113*, C08041, doi:10.1029/2007JC004681.

Ren, H.-L., and F.-F. Jin (2013), Recharge oscillator mechanisms in two types of ENSO, *J. Clim.*, *26*, 6506–6523, doi:10.1175/JCLI-D-12-00601.1.

Roundy, P. E., and G. N. Kiladis (2006), Observed relationships between oceanic Kelvin waves and atmospheric forcing, *J. Clim.*, *19*, 5253–5272.

Roundy, P. E., and J. R. Kravitz (2009), The association of the evolution of intraseasonal oscillations to ENSO phase, *J. Clim.*, *22*, 381–395.

Seiki, A., and Y. N. Takayabu (2007), Westerly wind bursts and their relationship with intraseasonal variations and ENSO. Part II: Energetics over the Western and central Pacific, *Mon. Weather Rev.*, *0072*, 3346–3361.

Seo, K., and Y. Xue (2005), MJO-related oceanic Kelvin waves and the ENSO cycle: A study with the NCEP Global Ocean Data Assimilation System, *Geophys. Res. Lett.*, *32*, L07712, doi:10.1029/2005GL022511.

Shinoda, T., P. E. Roundy, and G. N. Kiladis (2008), Variability of intraseasonal Kelvin waves in the equatorial Pacific Ocean, *J. Phys. Oceanogr.*, *38*, 921–944, doi:10.1175/2007JPO3815.1.

Takahashi, K., A. Montecinos, K. Goubanova, and B. Dewitte (2011), ENSO regimes: Reinterpreting the canonical and Modoki El Niño, *Geophys. Res. Lett.*, *38*, L10704, doi:10.1029/2011GL047364.

Takahashi, K., R. Martínez, A. Montecinos, B. Dewitte, D. Gutiérrez, and E. Rodriguez-Rubio (2014), TPOS White Paper #8a – Regional applications of observations in the eastern Pacific: Western South America. In Proceedings of the Tropical Pacific Observing System 2020 Workshop, A Future Sustained Tropical Pacific Ocean Observing System for Research and Forecasting, WMO and Intergovernmental Oceanographic Commission, La Jolla, Calif., 27–30 January. [Available at http://www.wmo.int/pages/prog/gcos/Publications/gcos-184_II.pdf.]

Torrence, C., and G. P. Compo (1998), A practical guide to wavelet analysis, *Bull. Am. Meteorol. Soc.*, *79*, 61–78.

Wang, W., M. Chen, A. Kumar, and Y. Xue (2011), How important is intraseasonal surface wind variability to real-time ENSO prediction?, *Geophys. Res. Lett.*, *38*, L13705, doi:10.1029/2011GL047684.

Wheeler, M. C., and G. N. Kiladis (1999), Convectively coupled equatorial waves: Analysis of clouds and temperature in the wavenumber-frequency domain, *J. Atmos. Sci.*, *56*, 374–399.

Xiang, B., B. Wang, and T. Li (2013), A new paradigm for the predominance of standing central Pacific warming after the late 1990s, *Clim. Dyn.*, *41*(2), 327–340, doi:10.1007/s00382-012-1427-8.

Xue, Y., M. Chen, A. Kumar, Z.-Z. Hu, and W. Wang (2013), Prediction skill and bias of tropical Pacific sea surface temperatures in the NCEP climate forecast system version 2, *J. Clim.*, *26*, 5358–5378.

Yeh, S.-W., S.-J. Kug, B. Dewitte, M.-H. Kwon, B. P. Kirtman, and F.-F. Jin (2009), El Niño in a changing climate, *Nature*, *461*, 511–514.

Yu, J. Y., and S.-T. Kim (2013), Identifying the types of major El Niño events since 1870, *Int. J. Climatol.*, *33*(8), 2105–2112.

Zhang, C. (2001), Intraseasonal perturbations in sea surface temperatures of the equatorial eastern Pacific and their association with the Madden-Julian Oscillation, *J. Clim.*, *14*, 1309–1322.